ORIGINAL PAPER

Magmatic evolution and post-crystallization hydrothermal activity in the early Cretaceous Pingtan intrusive complex, SE China: records from apatite geochemistry

Xiaobing Zhang[1,2] · Feng Guo[1,3] · Bo Zhang[1,2] · Liang Zhao[1,3] · Yangming Wu[1,2] · Guoqing Wang[1,2] · Melesse Alemayehu[1,4]

Abstract

We conducted in situ geochemical (major-, trace-element and Nd isotope compositions) analyses on apatite, together with whole-rock geochemistry from gabbro, granodiorite and granite in the Cretaceous Pingtan intrusive complex (SE China), aiming to investigate the roles of magmatic evolution and post-crystallization hydrothermal activity during its formation. Regardless of limited range in initial Nd isotopes ranges in both bulk rock [$\varepsilon_{Nd}(t) = -2.0$ to -0.4] and associated apatite [$\varepsilon_{Nd}(t) = -3.8$ to -0.4] from the Pingtan igneous complex, the apatite shows wide compositional and textural variations from gabbro to granite. Apatite from the gabbro (Group 1) displays a zoning structure characterized by increasing F and Sr but decreasing Cl and LREE from the core to rim. The increase of Sr from the core to rim is attributed to plagioclase accumulation, and the decreases of LREE and Cl from the core to rim is caused by post-crystallization hydrothermal activity. The high Cl content in the primitive Group 1 apatite further suggests derivation of the mafic magma from a mantle wedge metasomatized by Cl-rich sediment. In contrast, apatite from the granite (Group 2) has the lowest Cl and Sr but the highest F and Yb contents, which can be further divided into two subgroups of Group 2A and 2B based on texture and composition. Group 2A apatite shows homogenous composition with trace elements similar to apatite from I-type granite. The positive correlation between Sr and Eu/Eu* indicates that crystallization of Group 2A apatite is co-precipitated with a feldspar-dominated fractionation. However, Group 2B apatite contains mineral inclusion of monazite and has the highest U content and F/Cl ratio, resembling apatite from S-type or highly fractionated I-type granite. These features are consistent with the influence of post-crystallization hydrothermal activity. Apatite from the granodiorite (Group 3) has an intermediate composition between Group 1 and 2A apatite and shows a homogenous texture with trace element features similar to that from I-type granite. Group 3 apatite defined a negative correlation of Sr with La/Yb, which is attributed to fractional crystallization of hornblende and plagioclase. The geochemistry of apatite indicates that the gabbro and granitic rocks of the Pingtan intrusive complex were, respectively, derived from the mantle and crustal sources with similar $\varepsilon_{Nd}(t)$ values. Our study, therefore, demonstrates that apatite geochemistry has a potential to monitor the magma source, magmatic evolution and post-crystallization fluid activity of an igneous complex.

Keywords Magmatic evolution · Hydrothermal activity · Apatite geochemistry · Pingtan intrusive complex · SE China

Introduction

Apatite ($Ca_5 [PO_4]_3 [F, Cl, OH]$) is a common mineral in a wide range of rock types and the most abundant mineral reservoir of phosphate in the crust (e.g., Nash 1984; Piccoli and Candela 2002). It contains elements of various geochemical behaviors that are sensitive to the evolution of melt and fluid, such as halogens, rare earth elements (REEs), Sr, Y, Th and U (Bruand et al. 2017). Previous studies have suggested that apatite can be used as a powerful tool for unraveling complex

magmatic and post-crystallization hydrothermal activity (e.g., Boudreau et al. 1993; Sha and Chappell 1999; Bruand et al. 2014; Harlov 2015; Broom-Fendley et al. 2016b; Palma et al. 2019). More important, apatite crystallized from magma of different composition shows distinctive elemental geochemistry regardless of isotopic variation in the source protoliths (Sha and Chappell 1999; Belousova et al. 2001; Hsieh et al. 2008; Chu et al. 2009; Bruand et al. 2014; Teiber et al. 2014; Laurent et al. 2017). Accordingly, even in the case that the isotope data of magmas cannot be used to distinguish their sources, the geochemistry of associated apatite can still effectively record the fingerprint of magma source and possible magmatic and post-crystallization hydrothermal activity.

Southeastern (SE) China is characterized by a voluminous eruption of volcanic rocks and large-scale emplacement of coeval granitoids during Mesozoic. The magmas are predominantly felsic in composition with subordinate mafic counterparts (Zhou et al. 2006), which are always coeval and constitute mafic-to-felsic igneous complexes. In most cases, the mafic and felsic rocks show similar or even identical whole-rock isotopic compositions and have been termed as "equal-isotope" complexes (Xing et al. 1998). By contrast, each rock type (especially for the felsic lithology) from these complexes shows a large variation in zircon Hf isotopes that may be ascribed to magma mixing, crustal assimilation, incongruent melting of crustal protolith or source heterogeneity (Griffin et al. 2002; Li et al. 2012; Villaros et al. 2012; Tang et al. 2014; Hammerli et al. 2018). It is difficult to determine which magmatic process was predominant in the formation of the Mesozoic igneous complex. Furthermore, the post-crystallization hydrothermal activity may also play a role in homogenization of whole-rock radiogenic isotopes (e.g., Poitrasson et al. 1998). Therefore, it is necessary to re-evaluate the roles of magmatic evolution and post-magmatic processes during the formation of these Mesozoic igneous complexes in SE China.

In this study, we perform a comprehensive in situ geochemical (major-, trace-element and Nd isotopic compositions) analyses on apatite, in combination with additional whole-rock geochemical data, from gabbro, granodiorite and granite in the Cretaceous Pingtan intrusive complex in Fujian province, SE China. These results enable us to investigate the magma sources and the role of magmatic/hydrothermal processes in the petrogenesis of the Pingtan complex and show the potential of apatite geochemistry to be a tracer for magmatic and post-magmatic evolution.

Geological background

SE China consists of Yangtze block in the northwest and Cathaysia block in the southeast, separated by the Jiangnan Orogenic Belt (e.g., Li et al. 2002; Zhang et al. 2013). It underwent extensive tectonic and magmatic activities during Mesozoic. The distribution of Mesozoic igneous rocks in this area is mainly controlled by several large-scale NE-trending faults such as the Zhenghe-Dafu and Changle-Nanao faults (Fig. 1, Zhou et al. 2006). The magmatic rocks consist of predominant felsic lavas with minor intrusive mafic rocks (Zhou et al. 2006; Guo et al. 2012). It has been widely considered that the formation of the Cretaceous magmatism in SE China was related to subduction of the paleo-Pacific Ocean (e.g., Zhou et al. 2006; Wang et al. 2013). The Cretaceous felsic rocks in this area are mainly composed of calc-alkaline granitic batholiths and felsic volcanic lavas, which show hybrid geochemical signatures of crust-mantle interaction (e.g., Griffin et al. 2002; Zhou et al. 2006). The contemporaneous mafic intrusive rocks are mainly hornblende gabbros, which show geochemical features similar to arc mafic cumulates (e.g., Li et al. 2014). The "crust-like" Sr–Nd–Pb isotopic signatures of the gabbroic intrusions suggest a mantle wedge source enriched by melts of subducted sediments (Zhang et al. 2019).

The early Cretaceous Pingtan intrusive complex is located at Pingtan Island in the coastal area of Fujian province (Fig. 1b). Results of in situ zircon U–Pb dating yielded an age ranging from 115 to 125 Ma (Dong et al. 1997; Li et al. 2018; Zhang et al. 2019). Given the uncertainties of the measurements and petrographic relationship between gabbro and granite, the Pingtan Complex ranging from mafic through intermediate to felsic rocks was emplaced contemporaneously in early Cretaceous (Xu et al. 1999). Our samples were collected from this complex and included the above-mentioned three rock types (Fig. 1b). In combination with our and previous studies on whole-rock samples, the mineral assemblage and key geochemical features of each rock type are summarized as follows:

(1) The gabbro is distributed at the central part of the complex (Fig. 1b), occurring as stock and dike or as enclaves within the granodiorite (Xu et al. 1999). It is composed mainly of plagioclase (~60%), hornblende (15–35%), clinopyroxene (5–15%) and accessory apatite, magnetite, titanite and zircon (Fig. 2a, b).

(2) The granite constitutes the main body of the complex (Fig. 1b). It consists of biotite-monzogranite and biotite-syenogranite with massive, medium- to coarse-grained allotriomorphic-granular textures. The major mineral assemblage includes plagioclase (10–15%), alkali feldspar (35–40%), quartz (30–40%) and minor biotite with accessory minerals such as Fe-Ti oxides, apatite and zircon (Fig. 2c, d).

(3) The granodiorite occurs either as an individual intrusion between the gabbro and granite or as quenched enclaves within the granite (Xu et al. 1999). The mineral assemblage includes plagioclase (~60%), alkali
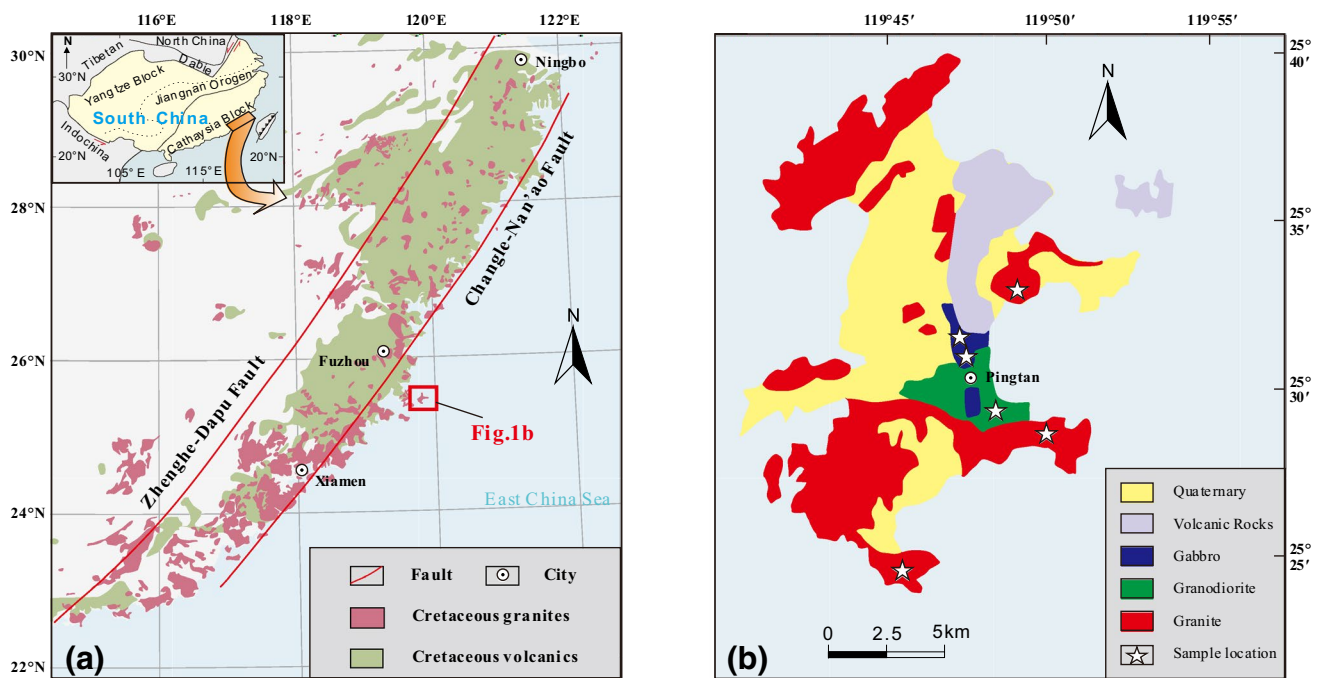
Fig. 1 Simplified geological maps showing tectonic location (**a**, after Zheng et al. 2013), distribution of late Mesozoic granites and volcanic rocks in the coastal region of SE China (**a**, after Zhou et al. 2006), and Pingtan intrusive complex (**b**, after Griffin et al. 2002)

feldspar (~ 20%), quartz (10–15%) and minor biotite (~ 5%) and accessory apatite and zircon (Fig. 2e, f).

Analytical techniques

Whole-rock geochemical analyses

Whole-rock major oxides were determined by wavelength X-ray fluorescence spectrometry (XRF) at Australian Laboratory Service Group. About 0.5 g of each sample powder was thoroughly mixed with 3.6 g $Li_2B_4O_7$, 0.4 g LiF, 0.3 g NH_4NO_3, and minor LiBr in a platinum crucible. It was then melted in a furnace to form a glass disk for major element analysis. Trace element concentrations of the samples were determined by a Perkin-Elmer ELAN 6000 inductively coupled plasma mass spectrometry (ICP-MS) after acid digestion in high-pressure Teflon bombs at Guangzhou Institute of Geochemistry (GIG), Chinese Academy of Sciences (CAS). During the course, ~ 50 mg sample powder was mixed with 1 mL HF and 0.5 mL HNO_3 in a Teflon beaker. Then the Teflon beaker was sealed in a stainless-steel bomb and heated at 190 °C for 48 h. The more detailed analytical procedure was reported by Liu et al. (1996). The analytical errors were 5% for rare earth element (REE) and high field strength element (HFSE), and 5 to ~ 10% for the other elements, based on repetitive analyses of USGS standards GSR-1 (granite), GSR-2 (andesite) and GSR-3 (basalt).

Whole-rock Sr and Nd isotope analyses were performed with a Finnigan Neptune multi-collector ICP-MS at the GIG-CAS, following the analytical procedures described by Li et al. (2006). The Sr and REE were separated via cation columns, and Nd fractions were further separated by HDEHP-coated Kef columns. The procedural blanks were less than 200 pg for Sr and about 30 pg for Nd. The measured $^{87}Sr/^{86}Sr$ and $^{143}Nd/^{144}Nd$ ratios were normalized to $^{86}Sr/^{88}Sr = 0.1194$ and $^{146}Nd/^{144}Nd = 0.7219$, respectively. The reported $^{87}Sr/^{86}Sr$ and $^{143}Nd/^{144}Nd$ ratios were adjusted to the NBS SRM 987 standard ($^{87}Sr/^{86}Sr = 0.710247 \pm 8$, 2σ) and the JNdi-1 standard ($^{143}Nd/^{144}Nd = 0.512115 \pm 4$, 2σ, $n = 4$), respectively. Repeated analyses of NBS SRM 987 standard and the Shin Etsu JNdi-1 standard separate yielded mean values of 0.710247 ± 9 and 0.512115 ± 6 (2σ, $n = 3$). During the whole-rock Sr–Nd isotope analyses, the USGS reference BHVO-2 (basalt) yielded $^{87}Sr/^{86}Sr = 0.703475 \pm 8$ (2σ, $n = 6$), $^{143}Nd/^{144}Nd = 0.512981 \pm 5$ (2σ, $n = 6$), consistent with the recommended values reported in Weis et al. (2005). The whole-rock major and trace element data are presented in Table S1 and the Sr–Nd isotopic are summarized in Table S2.

In situ elemental analyses of apatite

The selected apatite grains were mounted in epoxy and polished down to near half section to expose internal structures. All microscopic observations and in situ
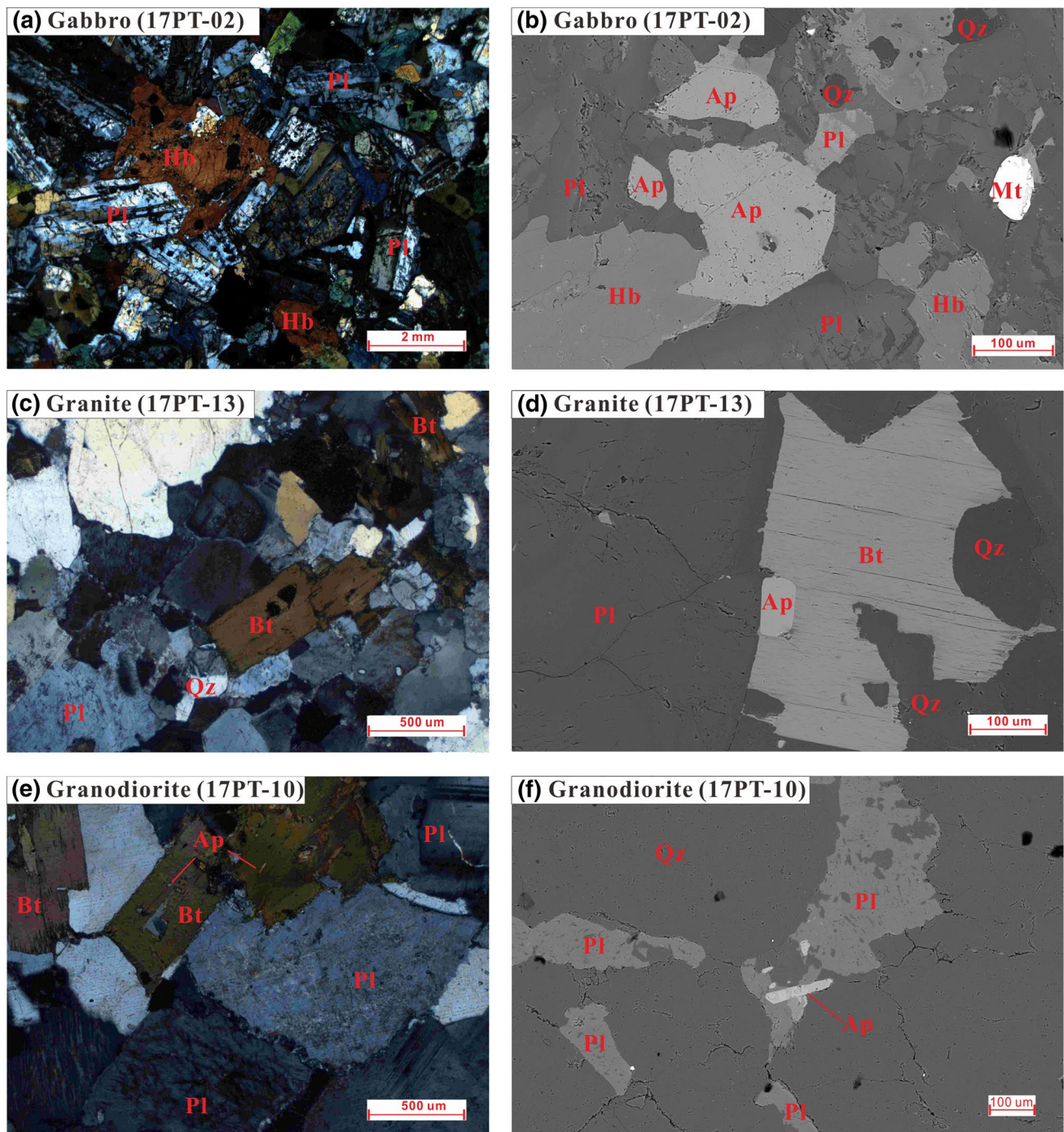
Fig. 2 Mineral assemblage of gabbro, granite and granodiorite in cross-polarized light and BSE images. **a** Plagioclase accumulation of the hornblende gabbro and **b** apatite with pores and inclusions. **c** Mineral assemblage of granite and **d** prismatic apatite inclusions in biotite. **e** Columnar apatite inclusions in biotite and **f** in feldspar from granodiorite. Mineral abbreviations: *Hb* hornblende, *Pl* plagioclase, *Bi* biotite, *Qz* quartz, *Ap* apatite, *Mt* magnetite

geochemical analyses on apatite were performed at GIG-CAS. Backscattered electron (BSE) images of the apatite were performed with a SUPRA 55 SAPPHIRE equipped with a secondary electron and energy-dispersive X-ray spectrometry (EDS) detectors. Maps of X-ray intensity for

apatite grains were obtained by electron probe microanalysis (EPMA) using a Cameca SX FiveFe instrument with operating conditions of 15 kV accelerating voltage and 50 nA beam current focused on 0.1–0.2 μm spot diameter.

The detection limits of the instrument for Ce, F and Cl are 300 ppm, 1400 ppm and 120 ppm, respectively.

The contents of major and minor elements in apatite have been determined by a JOEL JXA-8100 electron microprobe. The operating conditions were 15 kV accelerating voltage, 20 nA probe current, and 5 μm spot diameter with peak and background counting time of 7 s and 3 s for Na, 10 s and 5 s for F and Cl, 20 s and 10 s for Ca, P, Si, Fe and Mg, 60 s and 30 s for Mn, respectively. The standards for adjustment include apatite for Ca and P, fluorite for F, sodalite for Cl, albite for Na and Si and pyroxene for Mn, Fe, and Mg, respectively. The analytical errors were within 1%.

Trace-element analyses of apatite were performed with a resolution M-50 laser ablation (LA) system coupled to an Agilent 7900a type inductively coupled plasma-mass spectrometer (ICP-MS). The detailed analytical procedure was reported in Tu et al. (2011). The operating conditions were: 80 mJ laser energy, 6 Hz ablation frequency, and 31 μm laser ablation spot diameter. Helium gas carrying the ablated sample aerosol is mixed with argon carrier gas and both types of gas finally flow into ICP-MS. Each analysis included approximately 20 s of background acquisition (from a gas blank) followed by 45 s of data acquisition from the apatite. ^{43}Ca was used as the internal standard and the content of CaO was measured by EMPA. NIST SRM 610 was employed as an external standard, which was analyzed twice after every 8 sample analyses. Data reduction was performed off-line by the ICPMSDataCall software (version 10.0) (Liu et al. 2008). The major and trace element compositions of apatite are listed in Table S3. The mean trace element concentrations of NIST SRM 610 and NIST SRM 612 during this study and the recommended values (Pearce et al. 1997) are also listed in Table S3.

In situ Nd isotopic analyses of apatite

In situ Nd isotope analysis of apatite was performed on a Neptune Plus MC-ICP-MS (Thermo Scientific), coupled with a RESOlution M-50 193 nm laser ablation system (Resonetics). An X skimmer cone in the interface was utilized to improve the instrumental sensitivity. All isotope signals are recorded with Faraday cups under a static mode. The laser parameters were set as beam diameter of 82–112 μm, repetition rate of 6 Hz and energy density of ~ 4 J cm^{-2}. Helium was used as the carrier gas (800 ml min^{-1}). Each analysis consisted of 250 cycles with an integration time of 0.262 s per cycle. The first 29 s was used to detect the gas blank with the laser beam off, followed by 30 s laser ablation for sample signals collection with a laser beam on. During the measurement of this study, the gas blank of ^{143}Nd was less than 0.2 mV. The interferences of ^{144}Sm on ^{144}Nd was derived from the ^{147}Sm intensity with a natural ^{143}Sm/^{147}Sm = 0.20504 (Wasserburg et al. 1981). The mass

bias factor of Sm is calculated from the measured isotopic ratio of ^{147}Sm/^{149}Sm and its accepted value (1.08507, Wasserburg et al. 1981). The mass bias of ^{143}Nd/^{144}Nd was normalized to ^{146}Nd/^{144}Nd = 0.7129. The detailed instrumental conditions and data reduction procedure have been reported in Zhang et al. (2014, 2015). Every ten analyses of our apatite were followed by four analyses of Durango apatite standard and one analyses of McClure apatite standard. In situ Sm–Nd isotopic compositions of apatite are listed in Table S4. The twelve analyses of McClure apatite and 62 analyses of Durango apatite during this study yielded a weighted mean of ^{143}Nd/^{144}Nd = 0.512267 ± 0.000066 (2SD) and ^{143}Nd/^{144}Nd = 0.512489 ± 0.000039 (2SD), which are, respectively, consistent with the reported values (Yang et al. 2014). The mean Sm–Nd isotopic compositions of standards of Durango and McClure apatite during this study and the recommended values are also listed in Table S4 (Yang et al. 2014).

Results

Summary of whole-rock geochemistry

Our samples include gabbro, granodiorite and granite. The whole-rock geochemistry for the gabbro in this study has been comprehensively reported in Zhang et al. (2019). The gabbro (SiO$_2$ = 48–51 wt%) shows a calc-alkaline affinity (Fig. 3a) and is characterized by high Al$_2$O$_3$ and CaO, with similar trace element features to arc magmas (e.g., Pearce 1983; Wang 2002). They also have moderately enriched Sr–Nd isotopic features with ^{87}Sr/^{86}Sr$_{(i)}$ = 0.70553–0.70560, $\varepsilon_{Nd}(t)$ = − 1.6 to − 1.2 (Fig. 3d). The granites (SiO$_2$ > 71 wt%) are I-type granite (Fig. 3f), characterized by Na$_2$O > K$_2$O and moderately enriched Sr–Nd isotopic signatures (Fig. 3d, ^{87}Sr/^{86}Sr$_{(i)}$ = 0.70544–0.70554, $\varepsilon_{Nd}(t)$ = − 2.0 to − 1.7). The granodiorites (SiO$_2$ = 61–70 wt%) show transitional geochemical features between the gabbro and granite (Fig. 3a–c), with ^{87}Sr/^{86}Sr$_{(i)}$ = 0.70524–0.70564, $\varepsilon_{Nd}(t)$ = − 1.6 to − 0.7. Both the granite and granodiorite have similar Sr and Nd isotopic compositions to those of gabbro, and the three rock types tend to constitute an "equal-isotope" complex (Xing et al. 1998).

Texture of apatite

Representative BSE images and elemental mapping results for apatite from the Pingtan intrusive complex are presented in Figs. 4 and 5, respectively. Apatite grains from the gabbro (Group 1 from sample 17PT01 and 17PT02) are subhedral to anhedral and mostly coarse-grained in size (up to 0.5 mm, Figs. 4a, 5a). They commonly occur as inclusions hosted in other major phases such as hornblende, plagioclase and
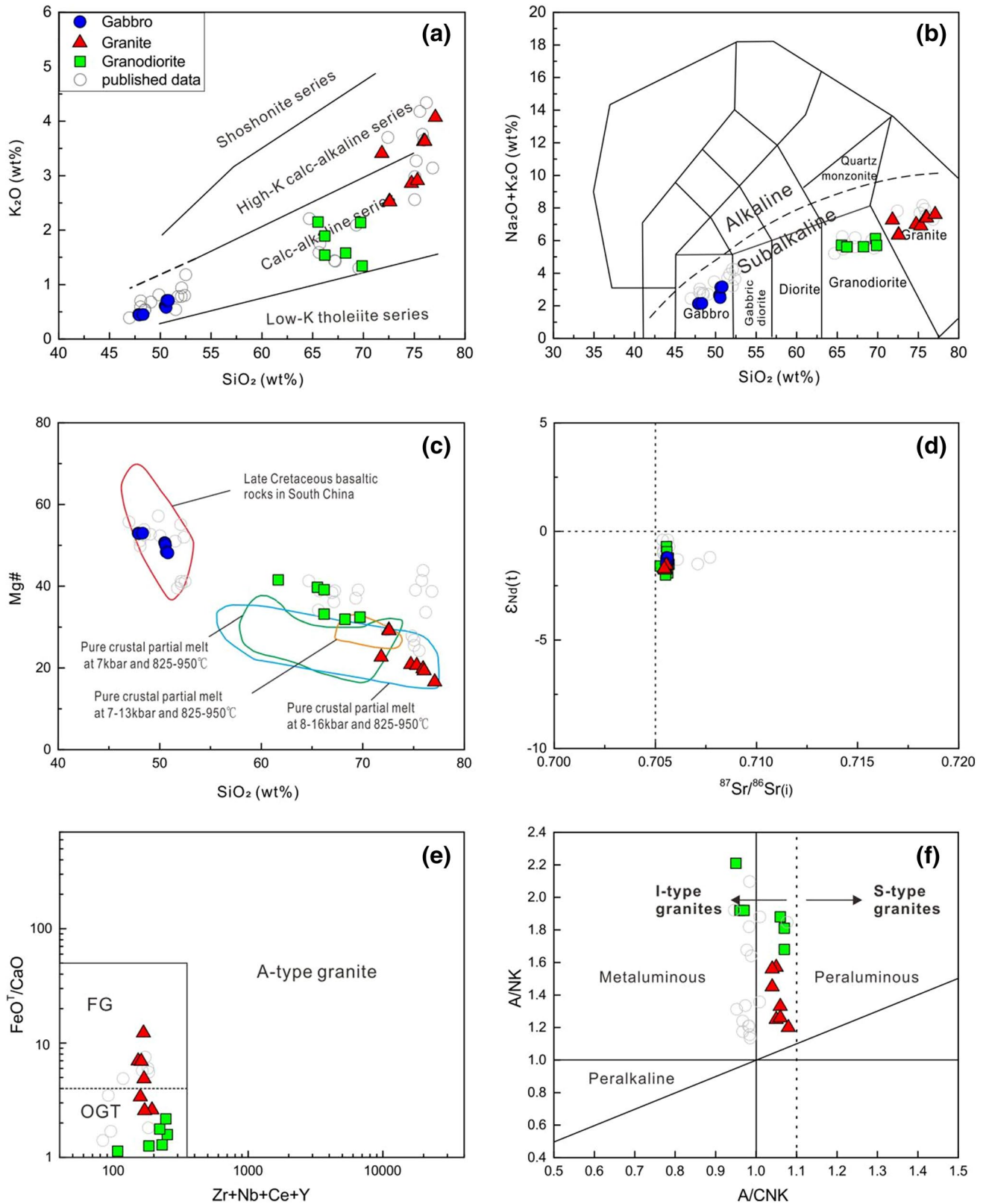
biotite (Fig. 2b), indicating that apatite is an early crystallizing phase. Only a few subhedral crystals show a homogeneous texture with a light grey color in BSE images, whereas the majority develop micro-pores and fractures (Figs. 2b, 4a, 5a). These pore-bearing crystals/domains are usually darker in BSE images and mostly occur on the grain rims

◀**Fig. 3** Geochemical diagrams of whole-rock samples from the Pingtan intrusive complex: **a** K_2O vs. SiO_2, **b** total alkali vs. silica (TAS), **c** Mg# vs. SiO_2, **d** $\varepsilon_{Nd}(t)$ vs. initial $^{87}Sr/^{86}Sr(i)$, **e** FeO^T/MgO vs. $Zr+Nb+Y+Ce$ (after Whalen et al. 1987) and **f** A/NK [molar $Al_2O_3/(Na_2O+K_2O)$] vs. A/CNK [molar $A1_2O_3/(CaO+Na_2O+K_2O)$]. In **a**, the boundaries of different rock series are from Peccerillo and Taylor (1976). In **b**, the classification scheme is from Middlemost (1994). In **c**, the variation fields show the previous experimental crustal melts: dehydration melting of low-K basaltic rocks at 8–16 kbar and 1000–1050℃ (Rapp and Watson, 1995), of moderately hydrous (1.7–2.3 wt% H_2O) medium- to high-K basaltic rocks at 7 kbar and 825–950 ℃ (Sisson et al. 2005), and of pelitic rocks at 7–13 kbar and 825–950 ℃ (Patiño Douce and Johnston 1991). Late Cretaceous basaltic rocks in South China (Yu et al. 2004; Cui et al. 2011). In **e**, FG = fractionated I- and S-type felsic granites; OGT = unfractionated I- and S-type granites. Symbols are shown in the figures. The other whole-rock geochemical data are listed in Table S1

or along with the fractures. The micro-pores are often filled with mineral inclusions like monazite, allanite and pyrite (Figs. 4a, 5a). The pore-free domains are observed at apatite cores and show homogenous textures with light grey color in BSE images.

Apatite grains from the granite (Group 2 from sample 17PT14, 17PT15 and 17PT16) are mostly prismatic coarse-grained crystals (up to 0.3 mm) and show homogeneous textures (Figs. 4b, 5b). They commonly occur as columnar inclusions hosted in plagioclase and biotite (Fig. 2d). They can be divided into two subgroups (Group 2A and 2B) in accordance with the textual difference. Group 2A apatite is homogenous with a light grey color in BSE images. In contrast, Group 2B apatite is relatively darker in BSE images and contains micro-pores and mineral inclusions (Figs. 4b, 5b). These mineral inclusions are mainly monazite and are also found along the edge of apatite (Fig. 4b). Apatite grains from the granodiorite (Group 3, from sample 17PT10, 17PT11 and 17PT12) are usually prismatic and exhibit relatively homogeneous textures (Figs. 2f, 4c, 5c). They commonly occur as columnar inclusions hosted in other major phases such as hornblende, plagioclase and biotite. Some grains also contain cracks and micro-pores filled with mineral inclusions like monazite (Fig. 4c). Elemental mapping of apatite from the gabbro, granodiorite and granite shows the compositional difference between pore-bearing and pore-free domains (Fig. 5a–c).

Chemical composition of apatite

Group 1 apatite is hydroxyapatite (Fig. 6b; Anthony 1990), which ranges from 54.5 to 57.9 wt% CaO and 40.1 to 42.7 wt% P_2O_5. It has the lowest F (0.59–1.12 wt%) and the highest Cl (0.71–1.73 wt%), with a negative correlation between F and Cl (Fig. 6a). Some apatite grains in Group 1 also show F and Cl zonation, with decreasing Cl and increasing F from the core to rim (Fig. 5a). The rim sections also have higher

Sr and lower LREE (e.g., Ce) concentrations than those of core (Fig. 4a).

Group 2 apatite is fluorapatite. Group 2A and Group 2B apatite have similar CaO and P_2O_5 contents. Compared to Group 2A, Group 2B apatite has lower Sr and La contents (Fig. 6d). In addition, Group 2B apatite has the highest U concentration (3.9–58.5 ppm) across the whole complex, while the other groups range from 1.0 to 9.4 ppm in U abundance.

Group 3 apatite is mainly fluorapatite and has CaO of 54.3–57.0 wt% and P_2O_5 of 41.4–43.3 wt%. It has variable F (1.33–2.36 wt%) and Cl contents (0.25–1.05 wt%) (Fig. 6a).

The apatite from the complex shows large ranges in both halogens and Sr content (92.3–690 ppm). Group 1 apatite has the highest Sr (436–690 ppm) and Group 2B apatite has the lowest content (92.3–227 ppm), whereas Group 2A and Group 3 apatite have medium Sr values of 227–479 ppm and 382–578 ppm, respectively. As shown in Fig. 6c–f, Sr shows negative correlations with Cl, La and ∑REE but a positive correlation with Yb in Group 1 apatite. With decreasing of Sr, Group 2A apatite shows increasing Yb and ∑REE but random variations in Cl and La, whereas Group 2B apatite shows an increase of Yb and decreases of La, ∑REE and Cl; Group 3 shows increasing La and ∑REE and decreasing Cl.

Group 1 apatite shows a wide range in ∑REE from 2068 to 3541 ppm (Fig. 6d, f). It is characterized by the strongest LREE/HREE fractionation (Fig. 7a) with the ratio of $(La/Yb)_N = 8.3–70.6$ and the weakest Eu negative anomaly (Eu/Eu* = 0.54–0.79). Group 2A apatite also shows a wide range of ∑REE from 4513 to 7757 ppm, especially in HREE such as Yb (36.2–208 ppm); While ∑REE contents of Group 3 apatite range from 2981 to 5092 ppm, with a relatively narrow Yb range (26.7–51.3 ppm) (Fig. 6e, f). Group 2A and Group 3 apatite also show right-declined REE distribution patterns (Fig. 7b, d), which are similar to apatite in I-type granite from the Lachlan Fold Belt (LFB, Fig. 7b, d, Sha and Chappell 1999). Compared with Group 1, Group 2A and Group 3 apatite have lower $(La/Yb)_N$ ratios (2.7–16.9) and stronger Eu negative anomaly (Eu/Eu* = 0.11–0.54). Group 2B apatite shows a similar ΣREE range (∑REE = 4513–8605 ppm) to Group 2A apatite (Fig. 6f). However, this group of apatite generally shows a near-flat REE distribution pattern that is similar to apatite from S-type or highly fractionated I-type granites in the LFB (Fig. 7c), with the weakest LREE/HREE fractionation (e.g., $(La/Yb)_N = 0.7–6.7$) but the strongest Eu negative anomaly (Eu/Eu* = 0.07–0.14).

In situ Nd isotopic compositions of apatite

All groups of apatite have similar Nd isotopic compositions (Fig. 8). Nd isotope ratios of Group 1 apatite range from 0.512385 to 0.512539, corresponding to an $\varepsilon_{Nd}(t)$
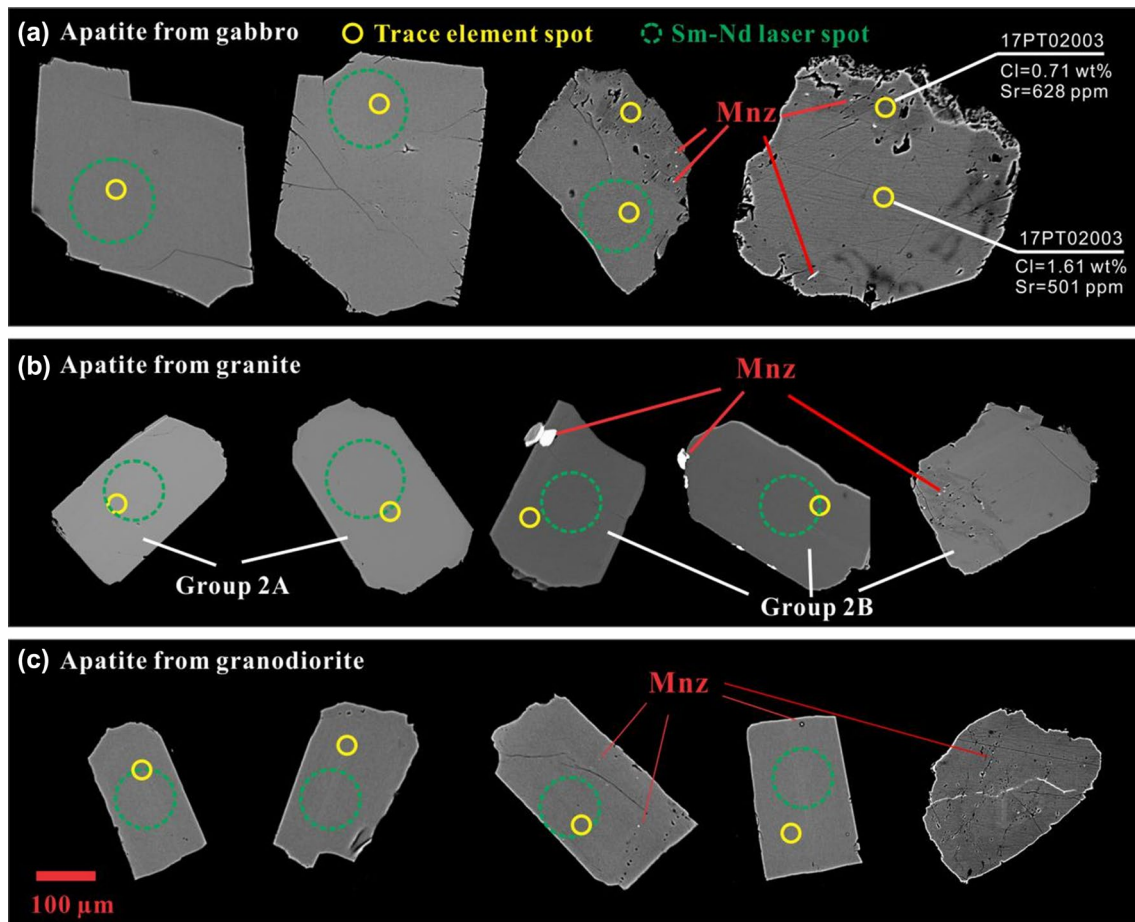
Fig. 4 Representative back-scattered electron (BSE) images of apatite from gabbro (**a**), granodiorite (**b**) and granite (**c**) in the Pingtan intrusive complex. *Mnz* monazite

range from − 3.4 to − 0.7 with an average of − 2.0 ($n = 30$, SD = 0.74). $^{143}Nd/^{144}Nd$ ratios of Group 2A apatite range from 0.512388 to 0.512567, corresponding to an $\varepsilon_{Nd}(t)$ range from − 3.8 to − 0.5 with an average of − 2.3 ($n = 40$, SD = 0.86). $^{143}Nd/^{144}Nd$ ratios of Group 2B apatite vary from 0.512440 to 0.512511, corresponding to an $\varepsilon_{Nd}(t)$ range from − 3.0 to − 1.7 with an average of − 2.3 ($n = 6$, SD = 0.57). $^{143}Nd/^{144}Nd$ ratios of Group 3 apatite vary from 0.512398 to 0.512568, corresponding to an $\varepsilon_{Nd}(t)$ range from − 3.7 to − 0.4 with an average of − 1.8 ($n = 40$, SD = 0.88). The variation range of average $\varepsilon_{Nd}(t)$ in apatite is almost identical to that of the whole-rock sample ($\varepsilon_{Nd}(t) = − 2.0$ to − 0.7) from which the apatite crystallized.

Discussion

The composition of apatite is primarily controlled by its host magma, and can be significantly modified by different magmatic processes (e.g., fractional crystallization and magma mixing) and post-crystallization hydrothermal processes

(e.g., Boudreau et al. 1993; Sha and Chappell 1999; Belousova et al. 2001; Chu et al. 2009; Bruand et al. 2014, 2016, 2017; Harlov 2015; McCubbin and Jones 2015; Bouzari et al. 2016; Palma et al. 2019). Regardless of limited $\varepsilon_{Nd}(t)$ ranges in both apatite and bulk rock (Figs. 3d, 8), the apatite shows wide compositional variations from the gabbro (Group 1) through granodiorite (Group 3) to granite (Group 2A and 2B). In the following sections, we will discuss the possible effect of the above-mentioned factors on the compositional variations observed in apatite from the Pingtan igneous complex.

Origin of apatite from the gabbro

Group 1 apatite is compositionally zoned in halogens and trace elements. These features can result from processes such as fractional crystallization, wall-rock contamination, magma mixing and post-crystallization fluid activity. Because F and Cl both behave as incompatible elements in olivine, pyroxene and plagioclase (Kendrick et al. 2014), fractionation of these minerals cannot result in increasing
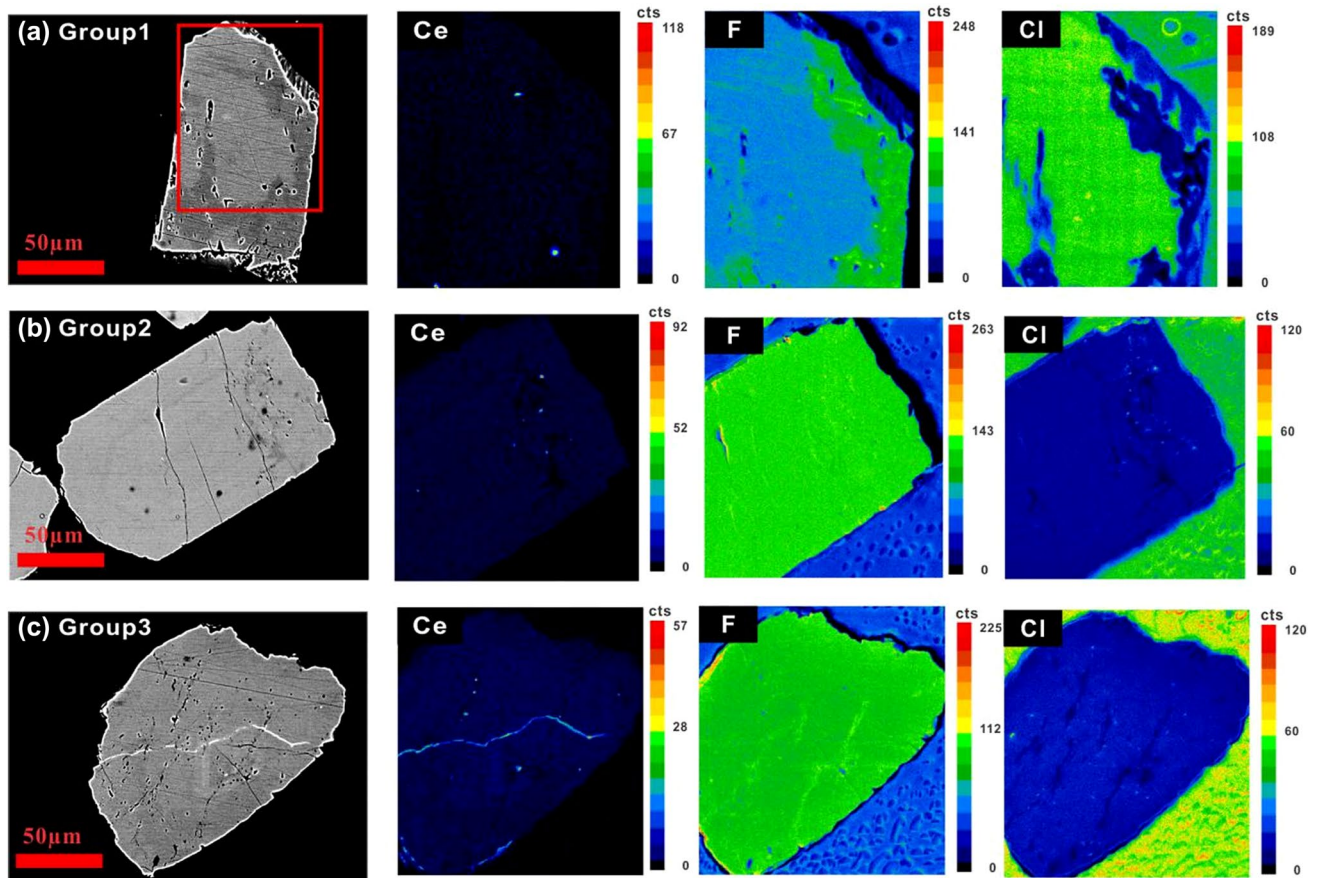
Fig. 5 BSE images and corresponding elemental mapping diagrams of representative apatite grains from gabbro (**a**), granite (**b**) and granodiorite (**c**) in the Pingtan intrusive complex. Note: the bright spots in Ce mapping correspond to the presence of monazite. The areas with relative F enrichment and Cl depletion reflect the effect of fluid activity in the micropores and along with the fractures

F and decreasing Cl from the core to rim in the crystallizing apatite (Fig. 5a). A hornblende-dominated fractionation may lead to halogen variation of the magma system (Van den Bleeken and Koga 2015) and possibly form the F and Cl zonation of apatite (Fig. 5a). However, apatite is an early crystallized phase in the Pingtan gabbro, in which it occurs as inclusions hosted in hornblende. Fractionation of hornblende may also lead to increasing Sr, La and La/Yb ratio in the differentiated magma (Tiepolo et al. 2007) and the resultant positive correlations of Sr with La and La/Yb in the coexisting apatite. This is inconsistent with the negative correlations between Sr and La and La/Yb in Group 1 apatite (Figs. 6d, 9a). Fractionation of a mafic mineral assemblage, such as olivine + pyroxene + plagioclase ± hornblende, therefore, cannot explain the geochemical variations in Group 1 apatite. In addition, Group 1 apatite generally displays lower Sr and higher Cl concentrations in the cores than the rims and shows a negative correlation between Sr and Cl (Figs. 4a, 5a, 6c), reflecting a role of simultaneous plagioclase accumulation during magmatic evolution (Zhang et al. 2019). However, because Sr is compatible but Cl and Yb are highly incompatible in plagioclase (Kendrick et al. 2014), accumulation of plagioclase would then result in increasing Sr but decreasing Cl and Yb in evolved magmas, creating negative correlations of Sr with both Cl and Yb in the corresponding apatite. This is also inconsistent with the negative correlation between Sr and Yb observed in Group 1 apatite (Fig. 6e). Finally, our previous study based on whole-rock and in situ plagioclase Sr-Pb isotopes has indicated that the processes of magma mixing and crustal assimilation played an insignificant role in the formation of the gabbro of Pingtan complex (Zhang et al. 2019). Accordingly, the elemental variation in Group 1 apatite cannot be produced only through magmatic processes. Alternatively, post-crystallization fluid activity could explain the wide ranges of REE, Cl and the pore/inclusion-bearing texture in Group 1 apatite, especially the strong variation in LREE and REE fractionation (Figs. 5c, 5d, 6a, 9a, 9b). Mineral inclusions, such as monazite found in the pore-bearing domains or along the fractures of apatite provide evidence for post-crystallization fluid activity (Figs. 4a, 5a; Harlov et al. 2002, 2005; Harlov 2015; Zirner et al. 2015). The remarkable difference
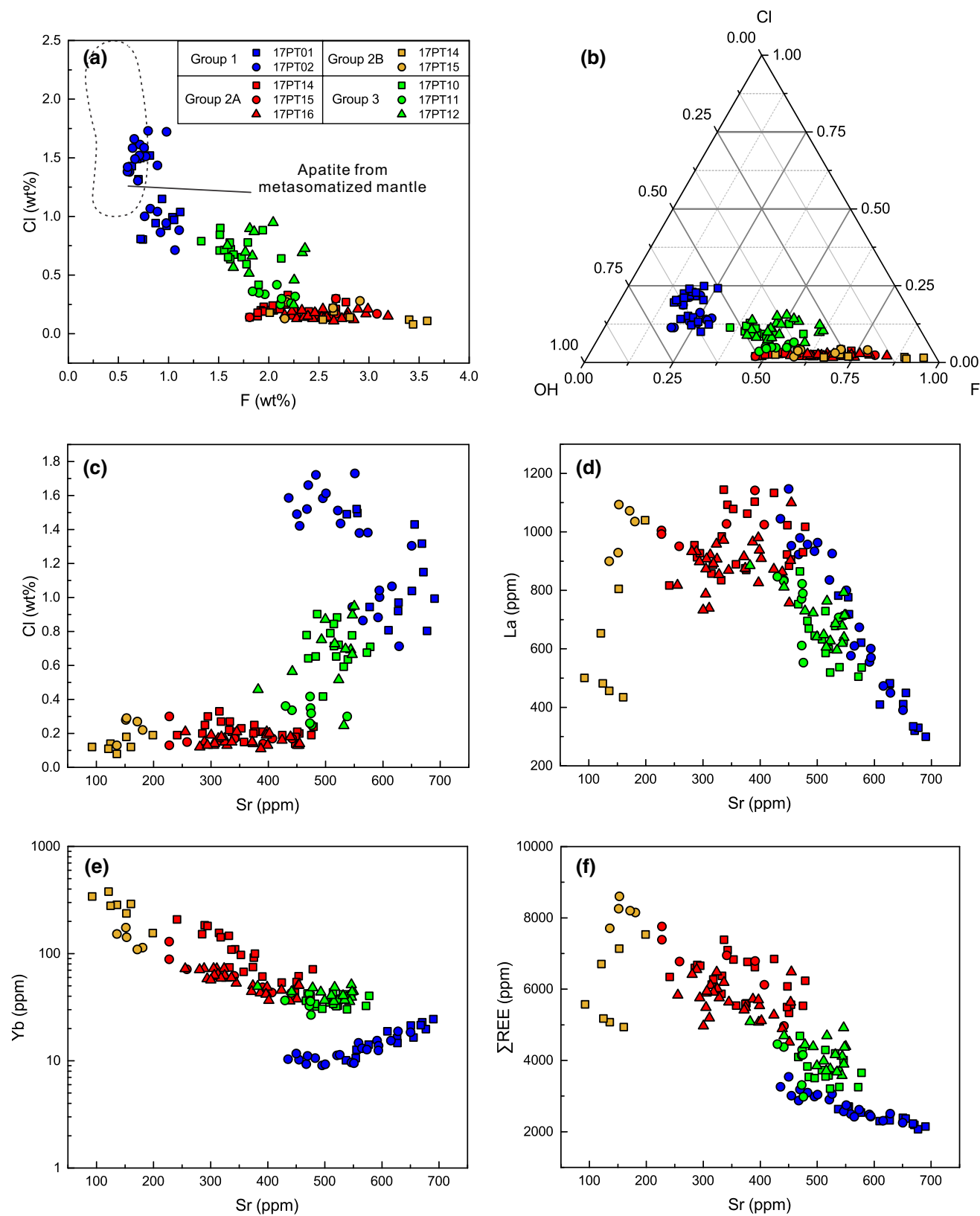
**Fig. 6** Plots of Cl vs. F (**a**), Cl–OH–F (**b**), Sr (ppm) vs. Cl (wt%, **c**), La (ppm, **d**), Yb (ppm, **e**) and ∑REE (ppm, **f**) of apatite from the Pingtan intrusive complex. In **a**, the field of apatite from the metaso-matized mantle is compiled from Patiño Douce et al. (2011). **b** The contents of volatile components (atomic proportions) in apatite is estimated using the method in Piccoli and Candela (2002)
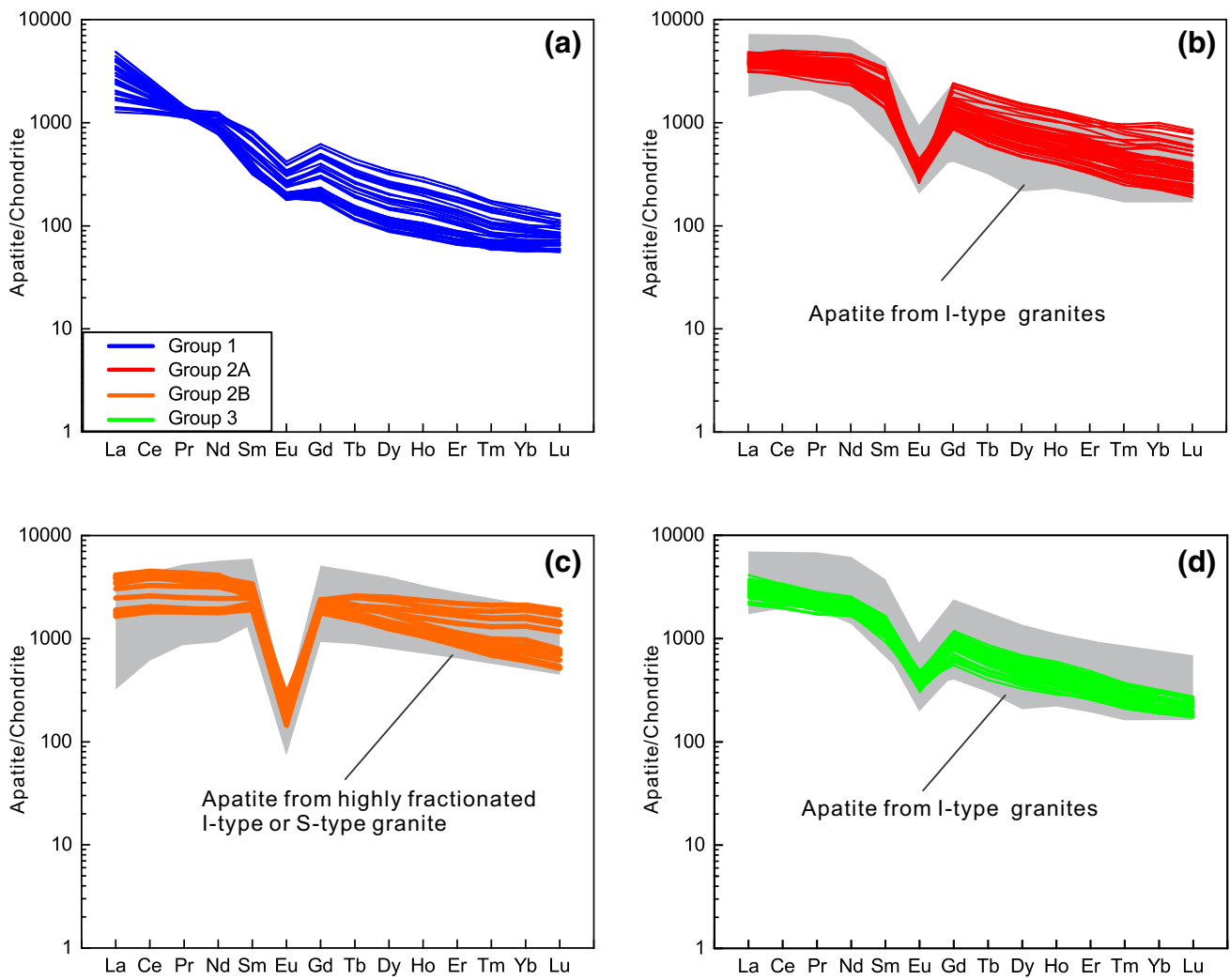
Fig. 7 Chondrite-normalized REE patterns of apatite from Group 1 apatite (**a**), Group 2A apatite (**b**), Group 2B apatite (**c**) and Group 3 apatite (**d**) in Pingtan intrusive Complex. Normalizing values are from McDonough and Sun (1995). The variation fields of S-type or highly fractionated I-type and I-type granite are from Sha and Chappell et al. (1999)
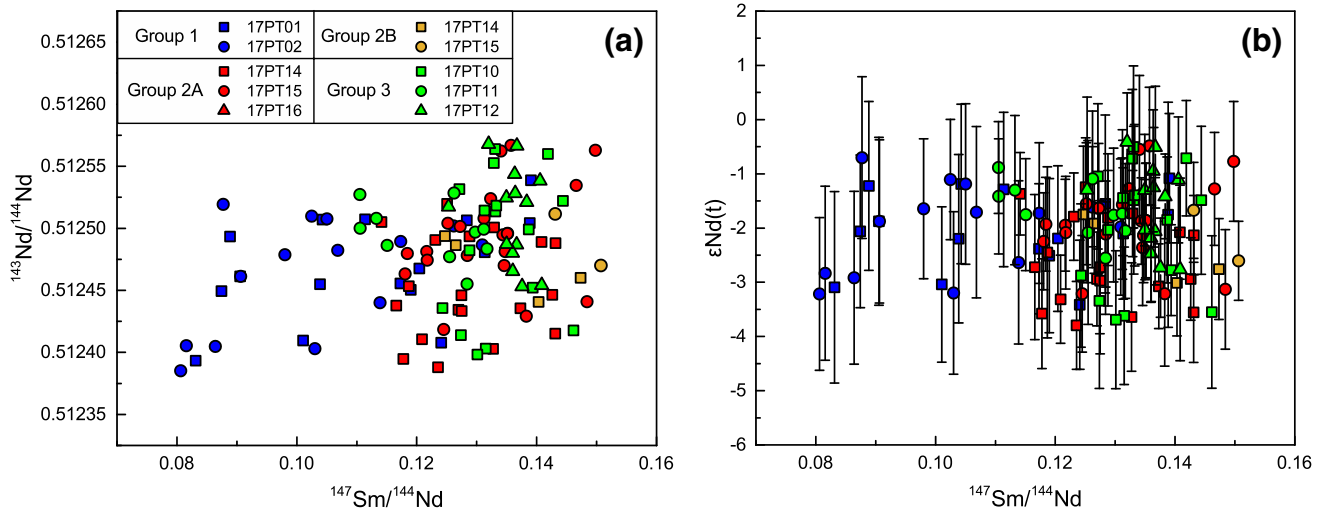
Fig. 8 Plot of $^{147}Sm/^{144}Nd$ versus $^{143}Nd/^{144}Nd$ (**a**) and ε_{Nd} (*t*) (**b**). The bars denote the analytical errors given as 2σ
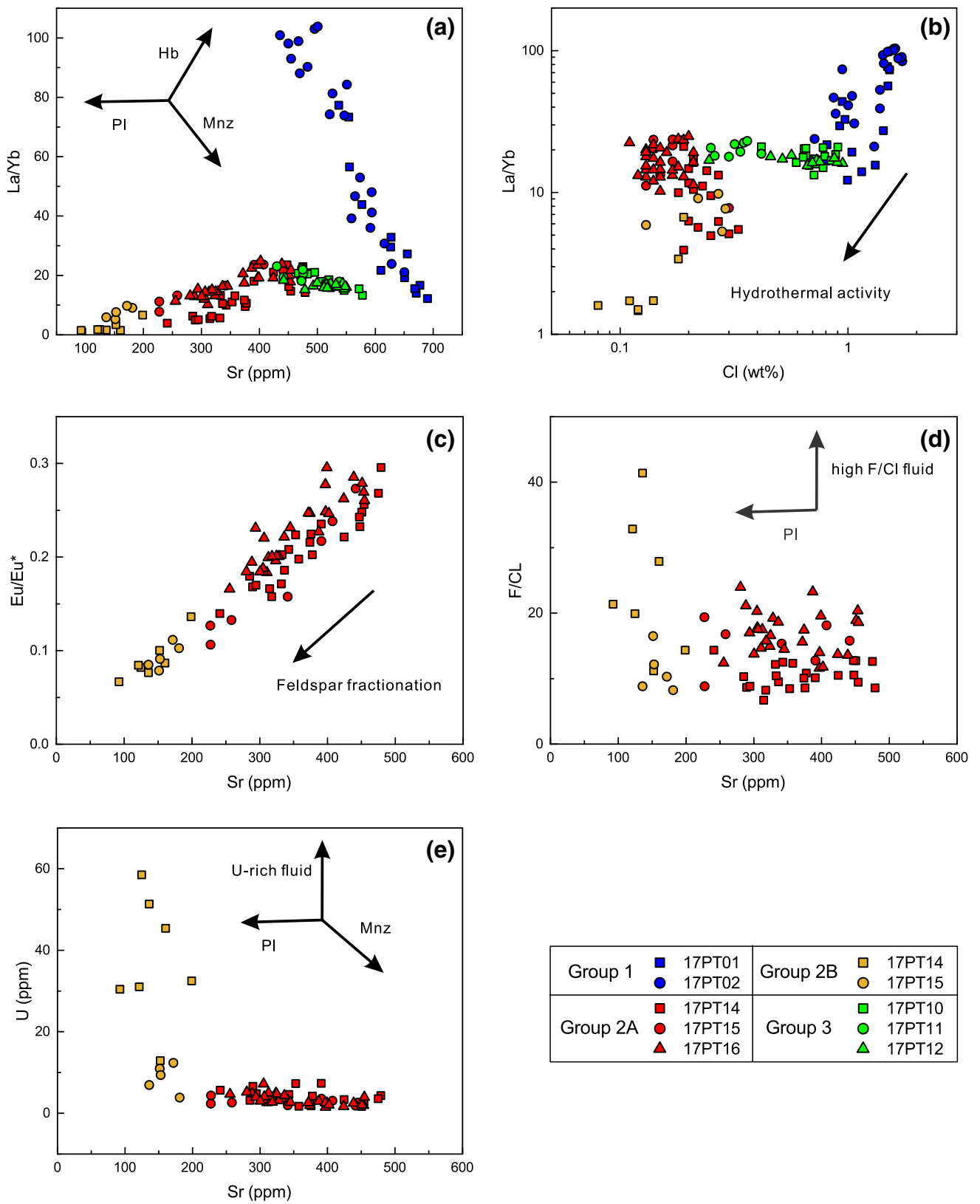
Fig. 9 Plots of Sr (ppm) vs. La/Yb (**a**), Cl (wt %) vs. La/Yb (**b**), Sr (ppm) vs. Eu/Eu* (**c**), Sr (ppm) vs. F/Cl (**d**) and Sr (ppm) vs. U (ppm, **e**) of apatite from the Pingtan intrusive complex

in F and Cl observed in Group 1 apatite can be interpreted by the interaction between apatite and hydrothermal fluid, since Cl preferentially partitions into the fluids (e.g., Webster et al. 2009; Zhang et al. 2012), whereas F strongly partitions into apatite from F-Cl bearing fluids even with low HF activities (e.g., Harlov 2015; Kusebauch et al. 2015a, b). Because chloride or fluoride complexes preferentially retain LREE instead of HREE (Migdisov et al. 2009; Williams-Jones et al. 2012; Broom-Fendley et al. 2016b), the hydrothermal fluids can fractionate LREE from HREE in the coexisting apatite (Broom-Fendley et al. 2016a, 2017). Therefore, the post-crystallization fluid activity is confirmed by the positive correlation between Cl and La/Yb in Group 1 apatite (Fig. 9b).

Although Group 1 apatite experienced post-crystallization alteration that may leach Cl, the core portions of some apatite grains preserve Cl up to 1.7 wt%. It has been suggested that the partitioning of Cl between apatite and melt is non-Nernstian and is a complex function of melt composition and Cl concentration of the magma (Webster et al. 2009; Doherty et al. 2014; Prowatke and Klemme, 2006). Experimental results suggested that Cl has a partition coefficient $D^{Ap/melt}$ Cl of ~ 0.8 in basaltic melts at 1066–1150 °C and 199–205 MPa (Mathez and Webster 2005). Considering the similarity of composition between the gabbro and experimental basaltic melt (Mathez and Webster 2005), it is reasonable to estimate the Cl content of melt based on the empirical relation ($D^{Ap/melt}$ Cl≈ 0.8) and the primary apatite (pore-free apatite). The calculated Cl concentration of the basaltic melt ranges from 1.5 to 2.1 wt%. This result is significantly higher than those of the primitive MORBs and primary arc magmas (Van den Bleeken and Koga 2015). Chlorine-rich apatite has been usually discovered in metasomatized lithospheric mantle (e.g., Griffin et al. 1988; Chazot et al. 1996; O'Reilly and Griffin 2000; Patiño Douce et al. 2011), such as that observed in Patagonian and Kamchatka mantle xenoliths (Laurora et al. 2001; Patiño Douce et al. 2011) (1.1–2.5 wt% Cl in apatite, Fig. 6a). In subduction zones, the subducted oceanic crust that experienced rock-seawater interaction contains high Cl content (e.g., Ito et al. 1983). Dehydration of the subducted oceanic crust will release Cl into the mantle wedge (e.g., Lassiter et al. 2002; Scambelluri et al. 2004). Hence, the upper mantle within or adjacent to subduction zones can be an ideal site for Cl enrichment. For example, Rowe and Lassiter (2009) attributed the chlorine enrichment in melt inclusions from the central Rio Grande Rift to shallow subduction of the Farallon plate. Sun et al. (2007) attributed the Cl enrichment relative to other incompatible elements such as K or Nb in back-arc lavas to transfer of Cl from the marine sediments to subarc mantle wedge via slab-derived melts or fluids. Correspondingly, we consider that the primary Cl-rich magma for the Pingtan gabbro was derived from a mantle metasomatized

by subducted marine sediment. This is consistent with our previous whole-rock geochemical studies that suggested the mantle source of the gabbro was enriched by melt from the subducted sediments (Zhang et al. 2019).

Origin of apatite from the granite

The two groups of apatite from the granite show compositional and textural variations. Group 2A apatite generally shows similar geochemical features to that from I-type granite, whereas Group 2B apatite shows similar compositions to that from S-type or highly fractionated I-type granite in the LFB (Fig. 7b, c; Sha and Chappell 1999). Because all Group 2B apatite grains were selected from the same samples as Group 2A apatite, the compositional variation from Group 2A to Group 2B apatite is mainly attributed to magmatic or post-crystallization hydrothermal processes.

The positive relationship of Sr and Eu/Eu* in Group 2 apatite indicates that the feldspar-dominated fractionation must have played a key role in the magmatic evolution (Fig. 9c). Ytterbium and ∑REE in Group 2A apatite increase with decreasing Sr (Fig. 6e, f), reflecting the influence of fractional crystallization (Ladenburger et al. 2016). Experimental results suggest that the partition coefficients of REE ($D^{Ap/melt}$ REE) between apatite and melt are strongly affected by the composition of the magma, i.e., $D^{Ap/melt}$ REE can be extensively increased following the increase of SiO_2 of the melt (Prowatke and Klemme 2006; Laurent et al. 2017). In a granitic system, feldspar fractionation would lead to decreasing Sr and increasing SiO_2 and REE in the evolved melt, and a resultant increase of $D^{Ap/melt}$ REE. Correspondingly, apatite crystallizing from the residual magma would contain high ∑REE and low Sr contents (Fig. 6f). On the other hand, fractional crystallization of plagioclase ± monazite ± allanite can create the positive correlation of Sr with La/Yb (Fig. 9a; Sha and Chappell 1999; Pan et al. 2016). Accordingly, the negative correlations of Sr versus Yb and ∑REE (Fig. 6e, f) and a positive correlation of Sr with La/Yb (Fig. 9a) in Group 2A apatite can be interpreted through a predominant feldspar fractionation during magmatic evolution.

Group 2B apatite has the highest ∑REE and lowest Sr content among the complex (Fig. 6f), suggesting its crystallization in a highly fractionated I-type granitic melt. At one hand, it shows significant decreases of La and ΣREE but increases of F/Cl and U (Figs. 6d, f, 9d, e) with decreasing Sr, which is inconsistent with feldspar fractionation. At the other hand, the strong HREE variation in the REE distribution patterns of Group 2B apatite (Fig. 7c) can be attributed to various degrees of mixing between the I-type granitic melt and an assumed highly fractionated I-type magma. However, this mixing cannot interpret the correlations of Sr versus La, Yb and ∑REE (Fig. 6d-f). For instance, the highest ∑REE content and lowest Sr of Group 2B apatite (Fig. 6f), suggest

that the assumed highly fractionated I-type granite should have contained the highest ∑REE and lowest Sr contents among the complex. The mixing between the I-type granitic magma for crystallization of Group 2A apatite and the assumed highly fractionated I-type granitic melt for Group 2B apatite would predict a negative correlation between Sr and ∑REE, but this contrasts with a broadly positive correlation between Sr and ∑REE (Fig. 6f). In summary, the geochemical variations in Group 2B apatite cannot be simply explained by magmatic processes. Instead, we suggest an important role of hydrothermal fluid in accordance with the following arguments.

1. The existence of some mineral inclusions such as monazite in Group 2B apatite (Figs. 4b, 5b) indicates hydrothermal fluid activity (Harlov and Förster 2003; Harlov et al. 2005; Harlov 2011; Zirner et al. 2015). The abundant monazite inclusion fills in the micro-pore or occurs as a vein along the micro-fracture of apatite, and is likely formed through fluid-induced dissolution–reprecipitation processes (Harlov and Förster 2003; Harlov et al. 2005; Harlov 2015; Zirner et al. 2015).
2. From Group 2A to Group 2B apatite, the U concentration increases rapidly (Fig. 9e), indicating the addition of oxidized U-rich fluid. The lack of U-rich granitic magmas in the study area favors a hydrothermal fluid to supply this U-rich material (e.g., Bali et al. 2011).
3. The positive correlation between Cl and La/Yb in Group 2B apatite indicates the role of post-crystallization fluid activity (Fig. 9b).
4. The F/Cl of Group 2B apatite increases remarkably with the decrease of Sr (Fig. 9d), indicating the interaction of apatite with high-F/Cl fluid after extensive feldspar crystallization.

In summary, Group 2A apatite was accompanied with feldspar-dominated fractionation within a granitic melt, whereas Group 2B apatite was influenced by post-crystallization hydrothermal activity. The geochemical similarity of apatite between highly fractionated I-type granite and S-type granite can be attributed to fluid-melt interaction (e.g., Sha and Chappell 1999; Hsieh et al. 2008; Chu et al. 2009).

Origin of apatite from the granodiorite

Group 3 apatite shows chemical composition transitional between Group 1 and Group 2A apatite but has almost identical $\varepsilon_{Nd}(t)$ values to the other groups (Figs. 6, 8), suggesting a relationship of fractional crystallization among the three rock types. However, fractionation of a mafic magma cannot interpret the geochemical features observed in the Pingtan complex. (1) The obvious whole-rock compositional gap between the gabbro and granitoids (including granodiorite

and granite) argues against a continuous fractional crystallization model to produce gabbro, granodiorite and granite. (2) The outcrop volume of the gabbro is quite small (< 10%) relative to that of granitoid (> 90%), which is inconsistent with a fractionation model that the mafic member generally has a much larger volume than the felsic component. And (3) the discontinuous compositional variations of apatite among the three rock types are also inconsistent with the trends defined by fractional crystallization (Figs. 6c–f, 9a).

In general, Group 3 apatite shows a closer affinity to Group 2A than Group 1 apatite, indicating a similar origin for both granodiorite and granite. Group 3 apatite shows a broad positive correlation between Cl and Sr (Fig. 6c). Such a feature may be attributed to (1) fractionation of Cl-rich minerals such as hornblende and biotite (Teiber et al. 2014; Ansberque et al. 2019). (2) Interaction with hydrothermal fluids, as observed in Group 2B apatite (Fig. 6c), and (3) addition of a Cl- and Sr-enriched mafic melt.

The parental magma of gabbro has much higher Cl and Sr contents and La/Yb than the granitic magma and can be a candidate for mafic component in the mixing process (e.g., Chu et al. 2009). However, a simple mixing between the gabbroic and granitic magmas should have produced positive correlations of Sr with Cl and La/Yb. This is inconsistent with the negative correlation of Sr with La/Yb observed in Group 3 apatite (Fig. 9a). Neither an effect of hydrothermal fluid activity can explain the relatively homogeneous texture with few mineral inclusions in Group 3 apatite (Figs. 4c, 7d).

Alternatively, the relationships of Sr with La/Yb and Cl indicate simultaneous crystallization of other HREE- and Cl-rich minerals accompanied by the formation of apatite (Figs. 6c, 9a). Strontium in apatite generally decreases in response to feldspar fractionation and would be an indicator of the magmatic evolution (e.g., Belousova et al. 2001; Bruand et al. 2017). Hornblende crystallization would lead to LREE enrichment and depletion of HREE and Cl in the residual melt (e.g., Tiepolo et al. 2007; Ansberque et al. 2019). Apatite crystallizing from such a residual melt will have high La/Yb and low Cl. Accordingly, the negative relationship between Sr and La/Yb and positive correlation of Sr with Cl in Group 3 apatite (Figs. 6c, 9a) can be interpreted by a fractional assemblage of hornblende and feldspar.

To synthesize the results from the whole-rock geochemistry and trace element and Nd isotope compositions of apatite, the gabbro and granitoids of the Pingtan igneous complex were, respectively, derived from enriched mantle and crustal sources with similar $\varepsilon_{Nd}(t)$ values. Following the subduction of Paleo-Pacific Ocean, the arc magmas formed by partial melting of the metasomatized mantle wedge underplated into the deep crust. Subsequent melting of the new accreted arc crust represented by the gabbro produced the felsic magma with an 'equal-isotope' feature. The crustal melt then experienced a fractional assemblage

of plagioclase and hornblende to form the granodiorite and underwent a feldspar-dominated fractionation to form the granitic magma. During the post-magmatic evolution, hydrothermal fluid was incorporated in both the mafic and granitic magma systems.

Conclusions

The in situ geochemical analyses show that the apatite from the Pingtan intrusive complex contains similar $\varepsilon_{Nd}(t)$ values but exhibits considerable textural and compositional variations among different rock types. The following conclusions can be summarized:

(1) Group 1 apatite is characterized by the highest Cl, Sr and La/Yb ratio but the lowest F and Yb concentrations, indicating its crystallization from a mafic magma that was derived from a mantle wedge metasomatized by subducted Cl-rich sediments. Compositional variations within this group reflect a combined result of plagioclase accumulation and post-crystallization hydrothermal fluid activity.

(2) Apatite from the granite can be divided into two subgroups. Group 2A apatite shows right-declined REE distribution patterns, resembling that of I-type granite. Group 2B apatite generally shows similar trace element characteristics to apatite from S-type or highly fractionated I-type granite. Both subgroups initially crystallized from a crustal melt with slightly negative $\varepsilon_{Nd}(t)$. The granitic magma experienced a feldspar-dominated fractionation to crystallize Group 2A apatite, whereas Group 2B apatite was further influenced by post-crystallization hydrothermal fluid activity. The proposed fluid-melt interaction may be one of mechanisms to explain the similar trace element features of apatite between highly fractionated I-type granite and S-type granites.

(3) Despite its composition transitional between Group 1 and Group 2A apatite, respectively, from the gabbro and granite, Group 3 apatite has a close affinity to that of granite. Its crystallization was accompanied by fractionation of hornblende and plagioclase in a crustal melt similar to the granitic magma.

(4) The combined geochemical results from the whole rock and apatite indicate the primary magmas for the gabbro and granitoid were, respectively, derived from the enriched mantle and crustal sources with similar Nd isotopic compositions. The 'equal-isotope' feature between the mafic and felsic components in the Pingtan igneous complex could be attributed to derivation of the granitic magma from the new accreted arc crust represented by the gabbro.

References

Ansberque C, Mark C, Caulfield JT, Chew DM (2019) Combined in situ determination of halogen (F, Cl) content in igneous and detrital apatite by SEM-EDS and LA-Q-ICPMS: a potential new provenance tool. Chem Geol 524:406–420

Anthony JW, Bideaux RA, Bladh KW, Nichols MC (1990) Handbook of mineralogy. Mineral Data Publ, Tucson

Bali E, Audétat A, Keppler H (2011) The mobility of U and Th in subduction zone fluids: an indicator of oxygen fugacity and fluid salinity. Contrib Mineral Petrol 161:597–613

Bau M (1996) Controls on the fractionation of isovalent trace elements in magmatic and aqueous systems: evidence from Y/Ho, Zr/Hf, and lanthanide tetrad effect. Contrib Mineral Petrol 123:323–333

Belousova EA, Walters S, Griffin WL, O'Reilly SY (2001) Trace-element signatures of apatites in granitoids from the Mt Isa Inlier, northwestern Queensland. Aust J Earth Sci 48:603–619

Boudreau AE, Love C, Hoatson DM (1993) Variation in the composition of apatite in the Munni Munni Complex and associated intrusions of the West Pilbara Block, Western Australia. Geochim Cosmochim Acta 57:4467–4477

Bouzari F, Hart CJR, Bissig T, Barker S (2016) Hydrothermal alteration revealed by apatite luminescence and chemistry: a potential indicator mineral for exploring covered porphyry copper deposits. Econ Geol 111:1397–1410

Broom-Fendley S, Brady AE, Wall F, Gunn G, Dawes W (2017) REE minerals at the Songwe Hill carbonatite, Malawi: HREE-enrichment in late-stage apatite. Ore Geol Rev 81:23–41

Broom-Fendley S, Heaton T, Wall F, Gunn G (2016a) Tracing the fluid source of heavy REE mineralisation in carbonatites using a novel method of oxygen-isotope analysis in apatite: the example of Songwe Hill, Malawi. Chem Geol 440:275–287

Broom-Fendley S, Styles MT, Appleton JD, Gunn G, Wall F (2016b) Evidence for dissolution-reprecipitation of apatite and preferential LREE mobility in carbonatite-derived late-stage hydrothermal processes. Am Mineral 101:596–611

Bruand E, Storey C, Fowler M (2014) Accessory mineral chemistry of high Ba–Sr granites from northern Scotland: constraints on petrogenesis and records of whole-rock signature. J Petrol 55:1619–1651

Bruand E, Storey C, Fowler M (2016) An apatite for progress: Inclusions in zircon and titanite constrain petrogenesis and provenance. Geology 44:91–94

Bruand E, Fowler M, Storey C, Darling J (2017) Apatite trace element and isotope applications to petrogenesis and provenance. Am Mineral 102:75–84

Chazot G, Menzies MA, Harte B (1996) Determination of partition coefficients between apatite, clinopyroxene, amphibole, and melt in natural spinel lherzolites from Yemen: Implications for wet melting of the lithospheric mantle. Geochim Cosmochim Acta 60:423–437

Chu M-F, Wang K-L, Griffin WL, Chung S-L, O'Reilly SY, Pearson NJ, Iizuka Y (2009) Apatite composition: Tracing petrogenetic processes in Transhimalayan granitoids. J Petrol 50:1829–1855

Cui Y, Xie Z, Wang B, Chen J, Yu Y, He J (2011) Geochemical characteristics of the late Mesozoic basalts in Southeastern Zhejiang Province and constraints on magma source materials. Geol J China Univ 17:492–512 **(In Chinese with English abstract)**

Doherty AL, Webster JD, Goldoff BA, Piccoli PM (2014) Partitioning behavior of chlorine and fluorine in felsic melt–fluid(s)–apatite systems at 50 MPa and 850–950 °C. Chem Geol 384:94–111

Dong CW, Zhou XM, Li HM, Ren SL, Zhou XH (1997) Late Mesozoic crust-mantle interaction in southeastern Fujian: isotopic evidence from the Pingtan igneous complex. Chinese Sci Bull 42:495–498

Griffin WL, O'Reilly SY (1988) Mantle metasomatism beneath western Victoria, Australia: II. isotopic geochemistry of Cr-diopside lherzolites and Al-augite pyroxenites. Geochim Cosmochim Acta 52:449–459

Griffin WL, Wang X, Jackson SE, Pearson NJ, O'Reilly SY, Xu XS, Zhou XM (2002) Zircon chemistry and magma mixing, SE China: in situ analysis of Hf isotopes, Tonglu and Pingtan igneous complexes. Lithos 61:237–269

Guo F, Fan W, Li C, Zhao L, Li H, Yang J (2012) Multi-stage crust–mantle interaction in SE China: temporal, thermal and compositional constraints from the Mesozoic felsic volcanic rocks in eastern Guangdong-Fujian provinces. Lithos 150:62–84

Harlov DE (2015) Apatite: a fingerprint for metasomatic processes. Elements 11:171–176

Harlov DE (2011) Formation of monazite and xenotime inclusions in fluorapatite megacrysts, Gloserheia granite pegmatite, Froland, Bamble Sector, southern Norway. Mineral Petrol 102:77–86

Harlov DE, Förster H-J (2003) Fluid-induced nucleation of (Y+REE)-phosphate minerals within apatite: Nature and experiment Part II Fluorapatite. Am Mineral 88:1209–1229

Harlov DE, Förster H-J, Nijland TG (2002) Fluid-induced nucleation of (Y + REE)-phosphate minerals within apatite: nature and experiment Part I Chlorapatite. Am Mineral 87:245–261

Harlov DE, Wirth R, Förster H-J (2005) An experimental study of dissolution–reprecipitation in fluorapatite: fluid infiltration and the formation of monazite. Contrib Mineral Petrol 150:268–286

Hammerli J, Kemp AIS, Shimura T, Vervoort JD, Dunkleyet DJ (2018) Generation of I-type granitic rocks by melting of heterogeneous lower crust. Geology 46:4

Hsieh PS, Chen CH, Yang HJ, Lee CY (2008) Petrogenesis of the Nanling Mountains granites from South China: Constraints from systematic apatite geochemistry and whole-rock geochemical and Sr–Nd isotope compositions. J Asian Earth Sci 33:428–451

Ito E, Harris DM, Anderson AT (1983) Alteration of oceanic crust and geologic cycling of chlorine and water. Geochim Cosmochim Acta 47:1613–1624

Kendrick MA, Jackson MG, Kent AJR et al (2014) Contrasting behaviours of CO2, S, H2O and halogens (F, Cl, Br, and I) in enriched-mantle melts from Pitcairn and Society seamounts. Chem Geol 370:69–81

Kusebauch C, John T, Whitehouse MJ, Engvik AK (2015a) Apatite as probe for the halogen composition of metamorphic fluids (Bamble Sector, SE Norway). Contrib Mineral Petrol 170:34

Kusebauch C, John T, Whitehouse MJ, Klemme S, Putnis A (2015b) Distribution of halogens between fluid and apatite during fluid-mediated replacement processes. Geochim Cosmochim Acta 170:225–246

Ladenburger S, Marks MAW, Upton B, Hill P, Wenzel T, Markl G (2016) Compositional variation of apatite from rift-related alkaline igneous rocks of the Gardar Province, South Greenland. Am Mineral 101:612–626

Lassiter JC, Hauri EH, Nikogosian IK, Barsczus HG (2002) Chlorine–potassium variations in melt inclusions from Raivavae and Rapa,

Austral Islands: constraints on chlorine recycling in the mantle and evidence for brine-induced melting of oceanic crust. Earth Planet Sci Lett 202:525–540

Laurent O, Zeh A, Gerdes A, Villaros A, Gros K, Slaby E (2017) How do granitoid magmas mix with each other? Insights from textures, trace element and Sr–Nd isotopic composition of apatite and titanite from the Matok pluton (South Africa). Contrib Mineral Petrol 172:80

Laurora A, Mazzucchelli M, Rivalenti G, Vannucci R, Zanetti A, Barbieri MA, Cingolani CA (2001) Metasomatism and melting in carbonated peridotite xenoliths from the mantle wedge: the Gobernador Gregores case (Southern Patagonia). J Petrol 42:69–87

Li X-H, Li Z-X, Wingate MTD, Chung S-L, Liu Y, Lin GC, Li W-X (2006) Geochemistry of the 755 Ma Mundine Well dyke swarm, northwestern Australia: part of a Neoproterozoic mantle super-plume beneath Rodinia? Precambrian Res 146:1–15

Li Z, Qiu JS, Xu XS (2012) Geochronological, geochemical and Sr–Nd–Hf isotopic constraints on petrogenesis of Late Mesozoic gabbro–granite complexes on the southeast coast of Fujian, South China: insights into a depleted mantle source region and crust–mantle interactions. Geol Mag 149:459–482

Li Z, Qiu JS, Yang XM (2014) A review of the geochronology and geochemistry of Late Yanshanian (Cretaceous) plutons along the Fujian coastal area of southeastern China: implications for magma evolution related to slab break-off and rollback in the Cretaceous. Earth Sci Rev 128:232–248

Li Z, Wang X-C, Wilde SA, Liu L, Li W-X, Yang X (2018) Role of deep-Earth water cycling in the growth and evolution of continental crust: constraints from Cretaceous magmatism in southeast China. Lithos 302–303:126–141

Li ZX, Li X, Zhou H, Kinny PD (2002) Grenvillian continental collision in south China: new SHRIMP U-Pb zircon results and implications for the configuration of Rodinia. Geology 30:163–166

Liu Y, Liu H-C, Li X-H (1996) Simultaneous and precise determination of 40 trace elements in rock samples using ICP–MS. Geochimica 25:552–558 **(In Chinese with English abstract)**

Liu Y, Hu Z, Gao S, Guenther D, Xu J, Gao C, Chen H (2008) In situ analysis of major and trace elements of anhydrous minerals by LA–ICP–MS without applying an internal standard. Chem Geol 257:34–43

Mathez EA, Webster JD (2005) Partitioning behavior of chlorine and fluorine in the system apatite-silicate melt-fluid. Geochim Cosmochim Acta 69:1275–1286

McCubbin FM, Jones RH (2015) Extraterrestrial apatite: planetary geochemistry to astrobiology. Elements 11:183–188

McDonough WF, Sun SS (1995) The composition of the Earth. Chem Geol 120:223–253

Middlemost EAK (1994) Naming materials in the magma/igneous rock system. Earth Sci Rev 37:215–224

ArtA M, Williams-Jones AE, Wagner T (2009) An experimental study of the solubility and speciation of the Rare Earth Elements (III) in fluoride- and chloride-bearing aqueous solutions at temperatures up to 300 °C. Geochim Cosmochim Acta 73:7087–7109

Nash WP (1984) Phosphate minerals in terrestrial igneous and metamorphic rocks. In: Phosphate minerals. Springer, Berlin, Heidelberg

O'Reilly SY, Griffin WL (2000) Apatite in the mantle: implications for metasomatic processes and high heat production in Phanerozoic mantle. Lithos 53:217–232

Palma G, Barra F, Reich M, Valencia V, Simon AC, Vervoort J, Leisen M, Romero R (2019) Halogens, trace element concentrations, and Sr–Nd isotopes in apatite from iron oxide-apatite (IOA) deposits in the Chilean iron belt: evidence for magmatic and hydrothermal stages of mineralization. Geochim Cosmochim Acta 246:515–540

Pan LC, Hu R-Z, Wang XS, Bi XW, Zhu JJ, Li C (2016) Apatite trace element and halogen compositions as petrogenetic-metallogenic

indicators: examples from four granite plutons in the Sanjiang region, SW China. Lithos 254:118–130

Patiño Douce AE, Johnston AD (1991) Phase equilibria and melt productivity in the pelitic system: implications for the origin of peraluminous granitoids and aluminous granulites. Contrib Mineral Petrol 107:202–218

Patiño Douce AE, Roden MF, Chaumba J, Fleisher C, Yogodzinski G (2011) Compositional variability of terrestrial mantle apatites, thermodynamic modeling of apatite volatile contents, and the halogen and water budgets of planetary mantles. Chem Geol 288:14–31

Pearce JA (1983) The role of sub-continental lithosphere in magma genesis at destructive plate margins. In: Hawkesworth CJ, Norry MJ (eds) Continental basalts and mantle xenoliths. Shiva, Nantwich, pp 230–249

Pearce NJG, Perkins WT, Westgate JA, Gorton MP, Jackson SE, Neal CR, Chenery SP (1997) A compilation of new and published major and trace element data for NIST SRM 610 and NIST SRM 612 glass reference materials. Geostand Newsl 21:115–144

Peccerillo A, Taylor SR (1976) Geochemistry of eocene calc-alkaline volcanic rocks from the Kastamonu area, Northern Turkey. Contrib Mineral Petrol 58:63–81

Piccoli PM, Candela PA (2002) Apatite in Igneous Systems. Rev Mineral Geochem 48:255–292

Poitrasson F, Paquette J-L, Montel J-M, Pin C, Duthou J-L (1998) Importance of late-magmatic and hydrothermal fluids on the Sm–Nd isotope mineral systematics of hypersolvus granites. Chem Geol 146:187–203

Prowatke S, Klemme S (2006) Trace element partitioning between apatite and silicate melts. Geochim Cosmochim Acta 70:4513–4527

Rapp RP, Watson EB (1995) Partitioning of lanthanides and Y between immiscible silicate and fluoride melts, fluorite and cryolite and the origin of the lanthanide tetrad effect in igneous rocks. J Petrol 36:891–931

Rowe MC, Lassiter JC (2009) Chlorine enrichment in central Rio Grande Rift basaltic melt inclusions: Evidence for subduction modification of the lithospheric mantle. Geology 37:439–442

Scambelluri M, Muntener O, Ottolini L, Pettke TT, Vannucci R (2004) The fate of B, Cl and Li in the subducted oceanic mantle and in the antigorite breakdown fluids. Earth Planet Sci Lett 222:217–234

Sha L-K, Chappell BW (1999) Apatite chemical composition, determined by electron microprobe and laser-ablation inductively coupled plasma mass spectrometry, as a probe into granite petrogenesis. Geochim Cosmochim Acta 63:3861–3881

Sisson TW, Ratajeski K, Hankins WB, Glazner AF (2005) Voluminous granitic magmas from common basaltic sources. Contrib Mineral Petrol 148:635–661

Sun WD, Binns RA, Fan AC, Kamenetsky VS, Wysoczanski R, Wei GJ, Hu YH, Arculus RJ (2007) Chlorine in submarine volcanic glasses from the eastern Manus basin. Geochim Cosmochim Acta 71:1542–1552

Tang M, Wang X-L, Shu X-J, Wang D, Yang T, Gopon P (2014) Hafnium isotopic heterogeneity in zircons from granitic rocks: Geochemical evaluation and modeling of "zircon effect" in crustal anatexis. Earth Planet Sci Lett 389:188–199

Teiber H, Marks MAW, Wenzel T, Siebel W, Altherr R, Markl G (2014) The distribution of halogens (F, Cl, Br) in granitoid rocks. Chem Geol 374:92–109

Teiber H, Marks MAW, Arzamastsev AA, Wenzel T, Markl G (2015) Compositional variation in apatite from various host rocks: clues with regards to source composition and crystallization conditions. Neues Jahrb Für Mineral Abh J Mineral Geochem 192:151–167

Tiepolo M, Oberti R, Zanetti A, Vannucciet R, Foley SF (2007) Trace-element partitioning between amphibole and silicate melt. Rev Mineral Geochem 67:417–452

Tu X, Zhang H, Deng W, Ling M, Liang H, Liu Y, Sun W (2011) Application of RESOlution in situ laser ablation ICP-MS in trace element analyses. Geochimica 40:83–98 **(In Chinese with English abstract)**

Van den Bleeken G, Koga KT (2015) Experimentally determined distribution of fluorine and chlorine upon hydrous slab melting, and implications for F–Cl cycling through subduction zones. Geochim Cosmochim Acta 171:353–373

Veksler IV, Dorfman AM, Kamenetsky M, Dulski P, Dingwell DB (2005) Partitioning of lanthanides and Y between immiscible silicate and fluoride melts, fluorite and cryolite and the origin of the lanthanide tetrad effect in igneous rocks. Geochim Cosmochim Acta 69:2847–2860

Villaros A, Buick IS, Stevens G (2012) Isotopic variations in S-type granites: an inheritance from a heterogeneous source? Contrib Mineral Petrol 163:243–257

Wang Y, Fan W, Zhang G, Zhang Y (2013) Phanerozoic tectonics of the South China Block: key observations and controversies. Gondwana Res 23:1273–1305

Wang ZH (2002) The origin of the Cretaceous gabbros in the Fujian coastal region of SE China: implications for deformation-accompanied magmatism. Contrib Mineral Petrol 144:230–240

Wasserburg GJ, Jacobsen SB, DePaolo DJ, McCulloch MT, Wen T (1981) Precise determination of SmNd ratios, Sm and Nd isotopic abundances in standard solutions. Geochim Cosmochim Acta 45:2311–2323

Webster JD, Piccoli PM (2015) Magmatic apatite: A powerful, yet deceptive, mineral. Elements 11:177–182

Webster JD, Tappen CM, Mandeville CW (2009) Partitioning behavior of chlorine and fluorine in the system apatite–melt–fluid. II: Felsic silicate systems at 200MPa. Geochim Cosmochim Acta 73:559–581

Weis D, Kieffer B, Maerschalk C, Pretorius W, Barling J (2005) High-precision Pb–Sr–Nd–Hf isotopic characterization of USGS BHVO-1 and BHVO-2 reference materials. Geochem Geophys Geosyst. https://doi.org/10.1029/2004GC000852

Whalen JB, Currie KL, Chappell BW (1987) A-type granites: geochemical characteristics, discrimination and petrogenesis. Contrib Mineral Petrol 95:407–419

Williams-Jones AE, Migdisov AA, Samson IM (2012) Hydrothermal mobilisation of the rare earth elements—a tale of "Ceria" and "Yttria". Elements 8:355–360

Xing G, Tao K (1998) The impact of Sr content on Sr isotope of magmatic rocks during crust-mantle interaction—an application to petrogenesis of cretaceous bimodal rocks in the coastal region of southeastern China. Volcanol Miner Resour 1:24–33 **(In Chinese with English abstract)**

Xu X-S, Dong C-W, Li W-X, Zhou X-M (1999) Late Mesozoic intrusive complexes in the coastal area of Fujian, SE China: the significance of the gabbro-diorite-granite association. Lithos 46:299–315

Yang Y-H, Wu F-Y, Yang J-H, Chew DM, Xie L-W, Chu Z-Y, Zhang Y-B, Huang C (2014) Sr and Nd isotopic compositions of apatite reference materials used in U–Th–Pb geochronology. Chem Geol 385:35–55

Yu X, Shu L, Yan T, Yu Y, Zu F, Wang B (2004) Geochemistry of basalts of late period of Early Cretaceous from Jiangshan-Guangfeng, SE China and its tectonic significance. Geochimica 33:465–476 **(In Chinese with English abstract)**

Zhang C, Holtz F, Ma C, Wolff PE, Li X (2012) Tracing the evolution and distribution of F and Cl in plutonic systems from volatile-bearing minerals: a case study from the Liujiawa pluton (Dabie orogen, China). Contrib Mineral Petrol 164:859–879

Zhang Y, Wang Y, Geng H, Zhang Y, Fan W, Zhong H (2013) Early Neoproterozoic (~850Ma) back-arc basin in the Central Jiangnan

Orogen (eastern South China): geochronological and petrogenetic constraints from meta-basalts. Precambrian Res 231:325–342

Zhang L, Ren Z-Y, Nichols ARL, Zhang Y-H, Zhang Y, Qian S-P, Liu J-Q (2014) Lead isotope analysis of melt inclusions by LA–MC–ICP–MS. J Anal At Spectrom 29:1393–1405

Zhang L, Ren Z-Y, Xia X-P, Li J, Zhang Z-F (2015) IsotopeMaker: a Matlab program for isotopic data reduction. Int J Mass Spectrom 392:118–124

Zhang B, Guo F, Zhang X, Wu Y, Wang G, Zhao L (2019) Early cretaceous subduction of Paleo-Pacific Ocean in the coastal region of SE China: petrological and geochemical constraints from the mafic intrusions. Lithos 334–335:8–24

Zhou X-M, Sun T, Shen W-Z, Shu L-S, Niu Y-L (2006) Petrogenesis of Mesozoic granitoids and volcanic rocks in south China: a response to tectonic evolution. Episodes 29(1):26–33

Zhao L, Guo F, Fan W, Li C, Qin X, Li H (2012) Origin of the granulite enclaves in Indo-Sinian peraluminous granites, South China and its implication for crustal anatexis. Lithos 150:209–226

Zirner ALK, Marks MAW, Wenzel T, Jacob DE, Markl G (2015) Rare earth elements in apatite as a monitor of magmatic and metasomatic processes: the Ilímaussaq complex, South Greenland. Lithos 228:12–22

Affiliations

Xiaobing Zhang[1,2] · Feng Guo[1,3] · Bo Zhang[1,2] · Liang Zhao[1,3] · Yangming Wu[1,2] · Guoqing Wang[1,2] · Melesse Alemayehu[1,4]

[1] State Key Laboratory of Isotope Geochemistry, Guangzhou Institute of Geochemistry, Chinese Academy of Sciences, Guangzhou 510640, China

[2] College of Earth and Planetary Sciences, University of Chinese Academy of Sciences, Beijing 100049, China

[3] Institutions of Earth Sciences, Chinese Academy of Sciences, Beijing, China

[4] Department of Applied Geology, School of Applied Natural Science, Adama Science and Technology University, P.O. Box 1888, Adama, Ethiopia